Chemosphere 352 (2024) 141315

Contents lists available at ScienceDirect

Chemosphere

journal homepage: www.elsevier.com/locate/chemosphere

Efficient photoelectrochemical real textile wastewater detoxification using photoanodes of C_3N_4–$BiVO_4$

Isabelle M.D. Gonzaga [a,*], Roger Gonçalves [a], Carlos H.M. Fernandes [a], Marcelo Assis [b], Ivo F. Teixeira [c], Lucia H. Mascaro [a]

[a] LIEC-Interdisciplinary Laboratory of Electrochemistry and Ceramics, Federal University of São Carlos, São Carlos, SP, 13565-905, Brazil
[b] Department of Analytical and Physical Chemistry, University Jaume I, Castelló, 12071, Spain
[c] Department of Chemistry, Federal University of São Carlos, São Carlos, SP, 13565-905, Brazil

HIGHLIGHTS

- The C_3N_4– $BiVO_4$ mixture showed better photoelectrocatalytic properties.
- The photocurrent of the C_3N_4– $BiVO_4$ is 1.5 mA cm^{-2}
- The charge mobility increses 10 times in the C_3N_4– $BiVO_4$ mixture.
- PhEC detoxification and 55 % TOC in 300 min using C_3N_4– $BiVO_4$ photoanode.

GRAPHICAL ABSTRACT

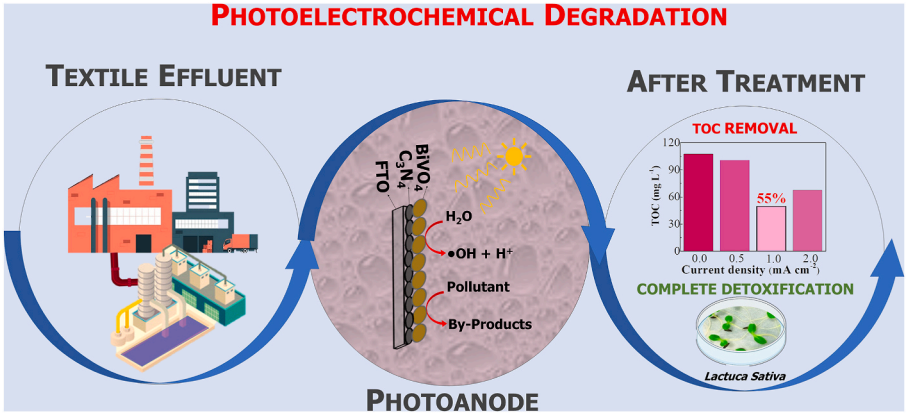

ARTICLE INFO

Handling editor: E. Brillas

Keywords:
Textile effluent
Photoelectrocatalysis
Carbon nitride
Heterostructures

ABSTRACT

Photoelectrochemical systems utilizing solar energy have garnered significant attention for their sustainability in remediating contaminated water. This study focuses on advancing photoanode development through the utilization of carbon nitrides (C_3N_4) and bismuth vanadate ($BiVO_4$), two promising semiconductor materials renowned for their efficient electron-hole pair separation leading to enhanced photocatalytic activity. Four distinct materials were synthesized and compared: $BiVO_4$ over C_3N_4, C_3N_4 over $BiVO_4$, and pristine $BiVO_4$ and C_3N_4. Upon electrochemical analysis, the C_3N_4–$BiVO_4$ heterostructure exhibited the highest photoelectrocatalytic charge transfer constant, mobility, and lifetime of charge carriers. Capitalizing on these exceptional properties, the composite was applied to remove organic matter real effluent from the textile industry. The photoelectrodegradation of the effluent demonstrated substantial removal of Total Organic Carbon (TOC) and the generation of low toxicity degradation products, accompanied by low energy consumption. The compelling results underscore the high potential of the synthesized C_3N_4–$BiVO_4$ heterostructure for industrial applications, particularly in addressing environmental challenges associated with textile industry effluents.

* Corresponding author.
E-mail address: bellemdg@gmail.com (I.M.D. Gonzaga).

https://doi.org/10.1016/j.chemosphere.2024.141315
Received 21 November 2023; Received in revised form 15 January 2024; Accepted 26 January 2024
Available online 27 January 2024

1. Introduction

Nowadays, wastewater volume grows along with the population boost, causing pollution to increase daily. Wastewater treatment plants (WWTP) are the main points of industrial waste discharge since they cannot efficiently remove most organic contaminants from industry, hospitals, and agriculture (Rodriguez-Mozaz et al., 2015). Therefore, many research groups have sought alternative methods to remove these contaminants (Gutierrez-Urbano et al., 2021).

Several types of treatment have been studied, such as adsorption (Zhuang et al., 2019), biological processes (Wang and Wang, 2018), and coagulation (Xu et al., 2021), but they have a high operating cost and low removal efficiency, which is why they have not been widely applied. (Wang and Zhuan, 2020). In such a way, advanced oxidative processes (AOP) have gained prominence since they can transform recalcitrant organic compounds into simple molecules with low environmental impact (Wang and Wang, 2019). Thus, the use of one or more AOPs has been widely studied. Among them, photoelectrochemistry, which combines light and electrical energies, has received great attention; this process aims to generate free radicals by photoactivation, which degrade organic pollutants (Gonzaga et al., 2021; Ma et al., 2022).

The use of semiconductors as photoanodes can be very promising since they can be low-cost materials and abundant in nature (Sharma et al., 2020). Usually, the photocatalytic efficiency depends on the catalyst's performance, which must have a small band gap for a wide range of light absorption, separation, efficient charge transport, and a strong redox capability (Sun et al., 2018). However, it is practically impossible to gather all these properties in a single catalyst (Yuan et al., 2021). To overcome these technology application limitations, several types of materials have been developed, such as the construction of semiconductor-semiconductor composites (Zhao et al., 2016), catalysts (Kang et al., 2019), doping (Zhong et al., 2020), and coupling with carbon materials (Ali et al., 2019).

Bismuth vanadate ($BiVO_4$) has high chemical stability, excellent photochemical properties, and a wide range of sunlight excitation. Therefore, it is a promising material for application in photoelectrochemistry (Corradini et al., 2020). However, the use of pure $BiVO_4$ has disadvantages, its poor electrical conductivity, sluggish surface kinetics, and the recombination of electron/hole pairs (Lu et al., 2019; Wang et al., 2022; Xie et al., 2023). On the other hand, carbon nitride (C_3N_4) has been extensively studied, as it is a metal-free semiconductor, environmentally friendly, easy to synthesize, and has interesting photocatalytic properties (Cao et al., 2015). Therefore, some studies about heterostructures based on $BiVO_4$ and C_3N_4 were previously reported in the literature. These have shown that the C_3N_4–$BiVO_4$ heterostructure facilitates the separation of photogenerated carriers with a promising photoelectrochemical performance (Karthik et al., 2020; Li et al., 2022; Wu et al., 2018). Although some researchers have evaluated this type of electrode and shown that it is promising, none have dedicated themselves to using it for the degradation of real effluents or detoxification, a relevant gap in the literature that must be filled.

Given this background, a C_3N_4–$BiVO_4$ heterostructured photoelectrocatalyst was prepared using a simple and fast method to remove organic matter and detoxify real effluent from the textile industry. The photoelectrocatalytic properties of the synthesized materials (C_3N_4, $BiVO_4$, $BiVO_4$–C_3N_4, and the C_3N_4–$BiVO_4$) were evaluated using a solar simulator. Furthermore, after the effluent degradation process, the reaction solutions' toxicity was first evaluated using the model with *Lactuca sativa* (*L. sativa*).

2. Experimental

2.1. Materials

All reagents used in this work were supplied by Sigma-Aldrich and used without prior purification. All aqueous solutions were prepared using ultrapure water (Milli-q). Electrochemical analyses were performed with a Methrom Potentiostat with Autolab NOVA 2.1 software. An effluent provided by a textile industry located in Araraquara, São Paulo, Brazil, was used for degradation tests, and Table S1 shows the characteristics of this effluent.

2.2. Photoanode synthesis

The synthesis of the $BiVO_4$ solution was performed as previously reported by Mascaro et al. (2014). The C_3N_4 was synthesized according to Silva et al. (2021) and later dissolved in PEG300 to prepare a precursor solution. Initially, the precursor solution was deposited by spin coating on a fluorine-doped tin oxide (FTO) electrode, pouring 30 μL of the solution into the FTO, and stirring at 2000 rpm for 30 s. Subsequently, the films were dried in an oven at 150 °C for 15 min, and this procedure was repeated 5 times, resulting in 5 layers. However, after the sixth and last layer was deposited, the modified electrode was placed in an oven for 30 min at 500 °C, with a heating rate of 10 °C min^{-1}, from the ambient temperature. This process was performed to improve the adhesion of the solution to the FTO and facilitate the crystallization of the expected oxides. With this, anodes with four different compositions are expected to be obtained: $BiVO_4$, C_3N_4, $BiVO_4$–C_3N_4, and C_3N_4–$BiVO_4$. Where the pure electrodes have six layers of a single material, the heterostructures were made by depositing three layers of each material.

2.3. Physical characterization

Diffuse reflectance spectroscopy (DRS) analyses were performed with a Cary 5E spectrophotometer, scanning from 300 to 800 nm. The x-ray diffractograms were obtained from the films on the substrate using a Shimadzu diffractometer model XRD6100 with CuKα radiation) 20° to 80° with a sweep speed of 2° min^{-1}. Raman spectra from 100 to 2000 cm^{-1} were obtained using a micro-Raman Horiba iHR550 with an excitation length of 532 nm (green laser) to study the samples' vibrational states.

Still, to evaluate the morphology of the materials synthesized in the samples, Scanning Electron Microscopy (SEM) images were performed using a FEI Inspect F50 model. To obtain Transmission Electron Microscopy images, the cathode of the mixture was placed in ultrasound with isopropanol for 30 min to then have the particles suspended and subsequently transferred to the diffraction grating, after which the images were obtained in a Jem-2100 Jeon equipment under an accelerating voltage of 200 kV coupled with an INCA energy TEM 200.

2.4. Electrochemical characterization and degradation experiments

The behavior of the photoanodes was evaluated on a three-electrode cell to perform the analyses. A Pt plate was used as the counter electrode, $Ag/AgCl/KCl_{sat}$ as the reference electrode, and the supporting electrolyte was 60 mM NaCl. Linear voltammetry was performed at 10 mV s^{-1}, with and without irradiation, using a solar simulator (with 100 mW cm^{-2} irradiance) as a light source. Electrochemical impedance spectroscopy (EIS) experiments were performed from 10 kHz down to 10 mHz with a signal amplitude of 10 mV_{rms}. The onset potential oxygen evolution reaction for each electrode with and without light. Mott-Schottky analysis was performed by measuring the impedance spectra of the samples over a potential range of 0.7–1.30 V vs. Ag/AgCl, with a potential step of −0.02 V at 1000 Hz. The same electrochemical system was also used to degrade the effluent from the textile industry, a volume of 70 mL varying the applied current (0.5, 1, and 2 mA cm^{-2}) for 300 min.

The effluent removal was evaluated using the total organic carbon (TOC) parameters measured in Sievers InnovOx 900-GE Analytical Instrument by taking 30 mL of the initial and after-degradation process solution. The TOC determination was carried out after mixing a diluted

volume of the treated sample with H_3PO_4 (6 M) and $Na_2S_2O_8$ (30 % m/V) solutions to determine the inorganic and total carbon, respectively. The TOC content was analyzed by subtracting the measured inorganic and total carbon values in terms of generated CO_2 (Fernandes et al., 2021; Renda et al., 2021).

The energy consumption (EC, in kWh (g TOC)$^{-1}$) was calculated according to Eq. (1), where E_{Cell} is the cell potential (V), I is the applied current intensity (A), t is the electrolysis time (s), V is the volume of the treated solution (L), and ΔTOC is the variation in the TOC removal (Garcia-Segura and Brillas, 2016);

$$EC = \frac{E_{Cell} \cdot I \cdot t}{V \cdot \Delta TOC} \quad (1)$$

2.5. Toxicity assessment

Photoelectrochemical treatment was evaluated for effluent toxicity before and after treatment using the method reported by Dória et al. (A. R. Dória et al., 2020a,b) using *L. sativa*. Briefly, the seeds were cleaned with sodium hypochlorite (4 % for 15 min) and then were washed with distilled water. Thus, 20 seeds were placed in Petri dishes with filter paper in contact with the analysis solutions and sealed for 5 days, kept at 22 ± 3 °C without any exposure to light. After 5 days, the number of seeds and roots was measured and used to calculate germination indices (GI) and relative growth indices (RGI).via Eqs. (2) and (3):

$$GI = \frac{RLS \; x \; NGS}{RLC \; x \; NGC} \; x \; 100 \quad (2)$$

$$RGI = \frac{RLS}{RLC} \; x \; 100 \quad (3)$$

Where, RSL and RLC were the relative root lengths of the sample and control, respectively. Also, the number of germinated seeds in the sample and those in the control are NGS and NGC, respectively.

3. Results and discussion

3.1. Morphological, structural, and optical characterization of photoanodes

The XRD patterns of the synthesized materials are shown in Fig. 1a. It is noticeable the characteristic peak of carbon nitride (27.6°) and the peaks of monoclinic $BiVO_4$ (28.9°, 35 and 47°)(Li et al., 2022). On the other hand, the main peaks of the pure materials were shifted for large angles in the materials containing C_3N_4 and $BiVO_4$, indicating the heterostructure formation. Alves et al., (2014), state that this displacement may be associated with interplanar spacing when considering larger

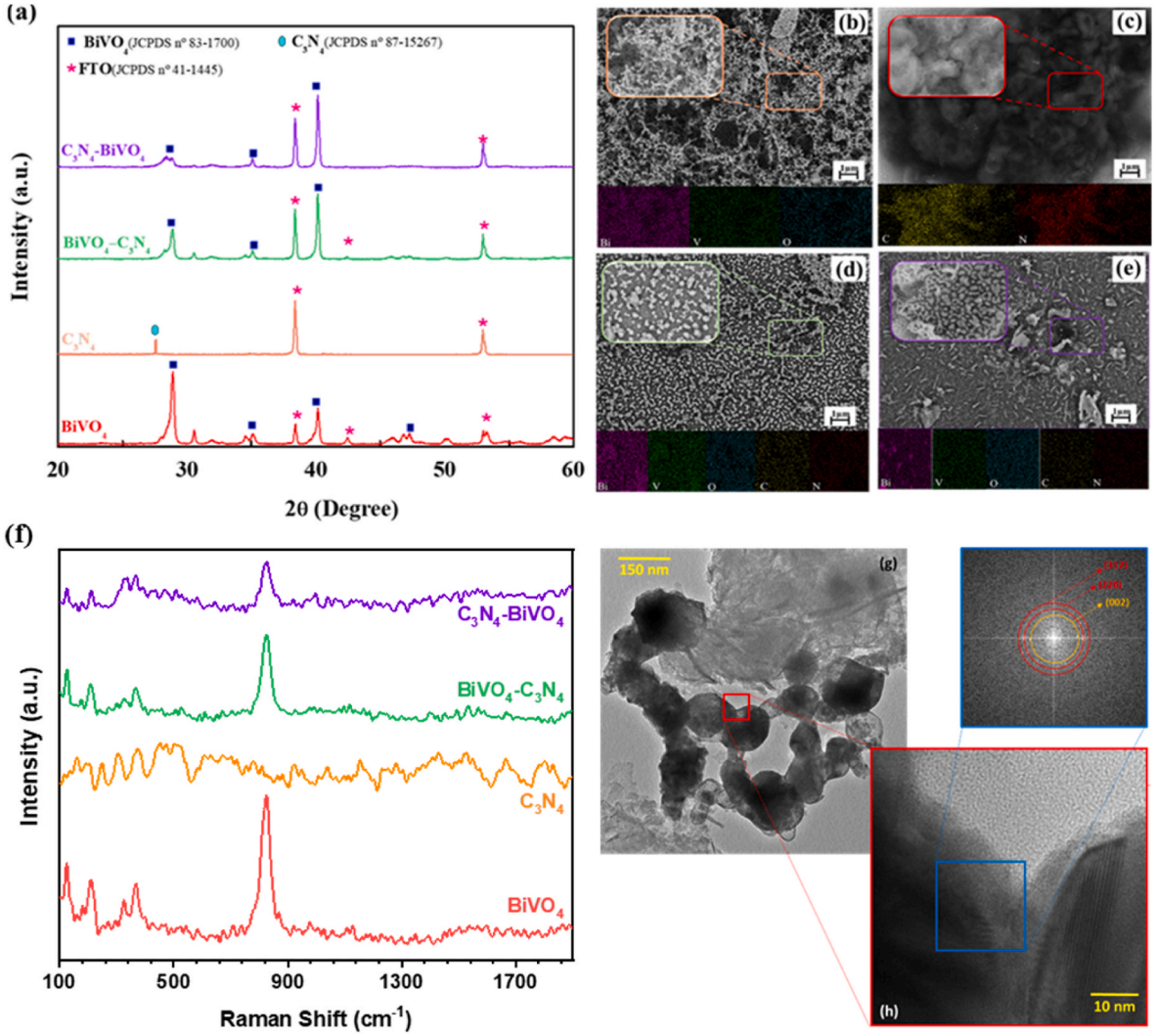

Fig. 1. (a) XRD diffraction patterns of synthesized photoanodes with different compositions after thermal treatments in the furnace; SEM images (b) $BiVO_4$, (c) C_3N_4, (d) $BiVO_4$–C_3N_4 and (e) C_3N_4–$BiVO_4$ of synthesized photoanodes at 2.5kx magnification (insets represent magnifications of 10kx), (f) Raman spectrum of the photoanodes, (g) Transmission electron microscopy (TEM) image and (h) High resolution TEM of the samples.

angles. Besides, the shift in the high-intensity peaks regarding the $BiVO_4$ suggests a preferential formation of a phase induced by the C_3N_4. Still, it was possible to observe that the relative intensities of the peaks are similar to those of the standard diffractogram. Araújo et al. (de Araújo et al., 2018) found equivalent results and concluded that there was no increase in the preference for $BiVO_4$ in the FTO since the relative intensities of the peaks in the synthesized material coincided with those of the standard diffractogram.

Scanning electron microscopies (SEM) were performed to analyze the photoanodes' morphology, as shown in Fig. 1b, c, d, and e. In Fig. 1b, the micrography of pure $BiVO_4$ is presented. In the insert of the figure, at a magnification of 10 kx, it is possible to observe that a granular morphology was formed. According to Gombroni et al. (Gromboni et al., 2016), this structure is promising, as it increases the active area and will probably be efficient in the presence of light. In Fig. 1c, the SEM image of pure C_3N_4 is observed; it is possible to state the morphology of crumpled paper. Similar morphology was also previously found by Gonçalves et al. (2018). Fig. 1d and e shows the micrographs obtained from the two heterostructures formed by $BiVO_4$–C_3N_4 and C_3N_4–$BiVO_4$, respectively. In both cases, the morphologies referring to $BiVO_4$ are mostly predominant. In the heterostructure where $BiVO_4$ is deposited first and then C_3N_4, decomposition probably occurred since this behavior is reported in the literature from 450 °C onwards (Silva et al., 2021). On the other hand, it is possible to notice a third morphology in the heterostructure where C_3N_4 is first deposited. It is probably a result of an aggregation of the two morphologies obtained in the pure materials, indicating the formation of the heterostructure.

The Raman spectra of the photoanodes excited by a green laser (533 nm) are shown in Fig. 1f. It is important to note that in all samples that have $BiVO_4$, the characteristic peaks of their vibrational bands: around 210, 380, 410, and 820 cm^{-1}. The structural information of $BiVO_4$ is given by the band centered at 210 cm^{-1}. The asymmetric and symmetric stretch of $[VO_4]$ tetrahedral clusters are given double bands at around 380 and 410 cm^{-1}, respectively. Finally, the stretching mode of V–O bonds is determined by the band centered at 810 cm^{-1}. Due to the power of the laser used, the C_3N_4 bands showed little definition, not appearing in samples with $BiVO_4$ (Thalluri et al., 2013; Yu and Kudo, 2006). However, it is possible to observe the bands centered at 700 and 1200 cm^{-1} due to their intensity in relation to the others (Cao et al., 2016; Gonçalves et al., 2018). Furthermore, a significant change in the relative intensity of the band at 210 cm^{-1} is noted, referring to the structural information of $BiVO_4$ in the presence of C_3N_4, suggesting that changes in the properties of the heterostructure may be due to structural changes at short-range in the photoactive heterostructure, in turn, the possible structural change corroborates the morphological changes observed in the SEM images.

To better observe the interactions of materials in the heterostructure, transmission images were obtained and are presented in Fig. 1g. It is possible to observe the C_3N_4 sheets that are almost completely transparent to electrons due to their small thickness, and on top of them are located the $BiVO_4$ nanoparticles. In the high-resolution region shown in Fig. 1h, where the contact between $BiVO_4$ nanoparticles is observed, the encapsulation of these particles with C_3N_4 sheets can be confirmed. Performing the fast Fourier transform (FFT) in this region allows the observation of the (312) and (220) planes, with interplanar distances of 2.58 and 1.88 Å, respectively, corresponding to $BiVO_4$. Additionally, the (002) plane of C_3N_4 with an interplanar distance of 3.36 Å is observed, confirming the formation of the heterostructure.

Fig. 2a shows the bandgap energy values (E_g) determined from the UV–Vis diffuse reflectance spectra (DRS), followed by the linear extrapolation of the Tauc plot curves. As a result, the E_g values for pure C_3N_4 and $BiVO_4$ were found to be 2.33 and 2.41 eV, respectively, which is in accordance with previously works(Cao et al., 2013; Liang et al., 2019; Pingmuang et al., 2017; Starukh and Praus, 2020). For the C_3N_4–$BiVO_4$ and $BiVO_4$–C_3N_4 heterostructures, slightly higher E_g values were obtained, 2.47 and 2.50 eV respectively. This behavior is due to the fact that, in addition to charge transfer between the atoms composing each pure material, there is charge transfer at the interface of both materials, which can cause variations in this value (Torabi and Staroverov, 2015).

Fig. 2b shows the Mott-Schottky plots for the photoanodes. Wherewith is it possible to find the flat-band potential (E_{fb}) and estimate the density of majority charge carriers using the Mott-Schottky equation, described in the Supplementary Information SI.1. The values obtained for $BiVO_4$ and C_3N_4 are that expected for the pure semiconductors (Aguilera-Ruiz et al., 2017; Wang et al., 2015). Based on E_{fb} and E_g, it was possible to construct the potential energy diagram for the samples, as illustrated in Fig. 2c. It was observed that the conduction band and the valence band of the heterostructures present more positive values compared to the corresponding bands of the pure materials. Therefore, when the heterostructures are illuminated with simulated sunlight, electronic transfer processes are altered by the interface between the semiconductors, allowing the excited electrons generated in the conduction band to be collected in the FTO.

Although the two pure materials present almost the same density charge carriers, it is known that C_3N_4 has much greater mobility than them, making it an excellent charge carrier. The observed faster movement of charge could favor the rapid separation of the photogenerated electron-hole pair in $BiVO_4$ at the interface, decreasing the recombination rate. Additionally, it is noticeable that the number of charge carriers density is found in very close values. This closeness in values might be expected, as natural variations could result in differences of hundreds or thousands, depending on the composite obtained. In this way, the improvement in the performance of the obtained heterostructured material is attributed to other factors, which will be described and discussed further on.

Table 1 summarizes the electronic parameters calculated by different optical and complementary electrochemical techniques. The E_{fb} and the E_{gap} information were used to obtain the band diagram of the materials. The illumination of material is useful for analyzing the charge transfer rate used to generate the necessary species for use in the degradation process (Bisquert et al., 2004). The quality of charge carriers also determines the photocatalytic efficiency of materials; the more durable and mobile they are, the better they utilize luminous excitation (Garcia-Belmonte et al., 2008). Therefore, if the recombination rate is low, the lifetime of the electron-hole pair is extended, making it more mobile and capable of reaching the solution electrode interface to react with the molecule of interest, resulting in a threefold increase (from 0.174 to 0.608 ms). Thus, a synergistic effect is observed in the mixture obtained between $BiVO_4$ and C_3N_4. Since carrier mobility is greater than that of $BiVO_4$, it leads to better current collection, contributing to less recombination of excitons. A more detailed explanation of these parameters and how to obtain them can be found in Supplementary Information SI.2.

According to Rohloff et al., (2019) the pristine $BiVO_4$ at $E_{fb} = 0.03$ V versus the reversible hydrogen electrode (RHE). On the other hand, Chowdhury et al., (2023) show $E_{fb} = 0.01$ V (RHE). In this work, the $E_{fb} = 0.035$V is among the previously reported values. Performance improvement strategies in the photocatalytic properties of materials involve adjusting the E_{fb} since this is important to verify the fermi level compatibility between the electrode and the molecule to be oxidized or reduced. Besides, an important feature of C_3N_4 is its easy modification of E_{fb} due to structural changes or doping, making it an excellent platform material for photocatalysis (Dong et al., 2014). This fact could also explain the band structure change in the heterostructured materials.

Subsequently, electrochemical characterizations were carried out to evaluate the performance of electrodes under illumination and in the dark when subjected to electrical polarization. Initially, linear voltammetry was carried out (Fig. 3a) in the presence and absence of light to obtain the materials' photocurrent density value in NaCl solution. It can be seen that pure C_3N_4 has no photocurrent (i.e. no photoelectrocatalytic activity). On the contrary, pure $BiVO_4$ presents a

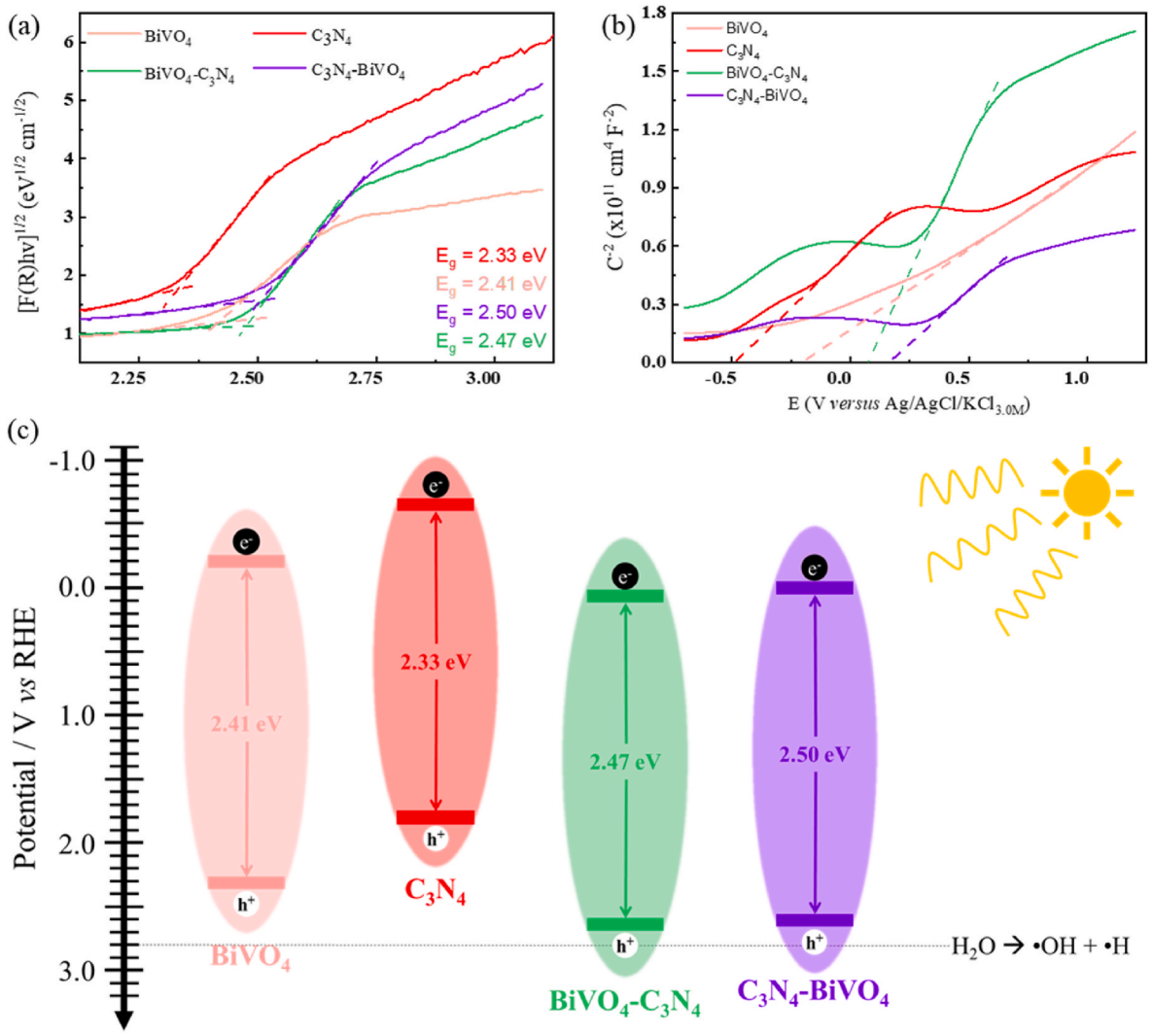

Fig. 2. (a) Tauc Plott, (b) Mott-Schottky plot, and (c)Band diagrams of the photoelectrodes.

Table 1
Calculated electronic properties for obtained materials.

Material	Bandgap (eV)	Flat-band potential (V vs. RHE)	Charge-transfer constant (s-1)	Majority charge carrier		
				Density ($\times 10^{17}$cm^{-3})	Mobility (cm^2 V^{-1} s^{-1})	Lifetime (ms)
$BiVO_4$	2.25	−0.006	77.6	2.03	1.09	0.174
C_3N_4	2.15	−0.441	172	1.97	1.60	0.255
$BiVO_4$–C_3N_4	2.37	0.144	256	1.61	0.307	0.049
C_3N_4–$BiVO_4$	2.35	0.109	275	3.42	3.80	0.608

significant photocurrent, achieving 0.9 mA cm^{-2} at 1.23 V vs. Ag/AgCl. After covering $BiVO_4$ with C_3N_4, the photocurrent of this material is similar to that of pure $BiVO_4$. On the other hand, when the order is reversed, *i.e.,* C_3N_4 is deposited first (C_3N_4–$BiVO_4$), the photocurrent significantly increases by about 1.6-fold at the same potential. This result is due to the fact that C_3N_4 has higher charge carrier mobility, reducing the recombination of electron/hole pairs, favoring the process in this deposition order. It is still possible to observe a negative shift in the photocurrent initiation potential of the heterostructures, corroborating the better photocatalytic efficiency compared to pure materials.

To elucidate the properties of these materials more completely, electrochemical impedance spectroscopy (EIS) with the presence and absence of light was performed (Fig. 3b and c). According to Li et al., a smaller semicircle arc in the Nyquist graph is related to lower resistance to electron transfer and an effective separation of the photogenerated electron-hole pairs (Li et al., 2015). Also, when evaluating the impedance data obtained, a simulation was performed using a combination of the ohmic resistance of the electrolyte (R_s) in series with the charge transfer resistance for the reaction in the material (R_{ct}), which is associated with the size of the semicircles formed and Q elements (may be related to capacitance) (Aline R. Dória et al., 2020a,b). Thus, the comparison between Fig. 3a and b is extremely important.

The impedance spectra of the materials with simulated solar irradiation show a smaller semicircular arc than those conducted in the dark. This behavior occurs due to a photogenerated current, which decreases resistance to charge transfer (Xie et al., 2019). Therefore, the greater the photocurrent, the decrease in arc size compared to the spectrum in the dark. Furthermore, the heterostructures have the smallest arc compared

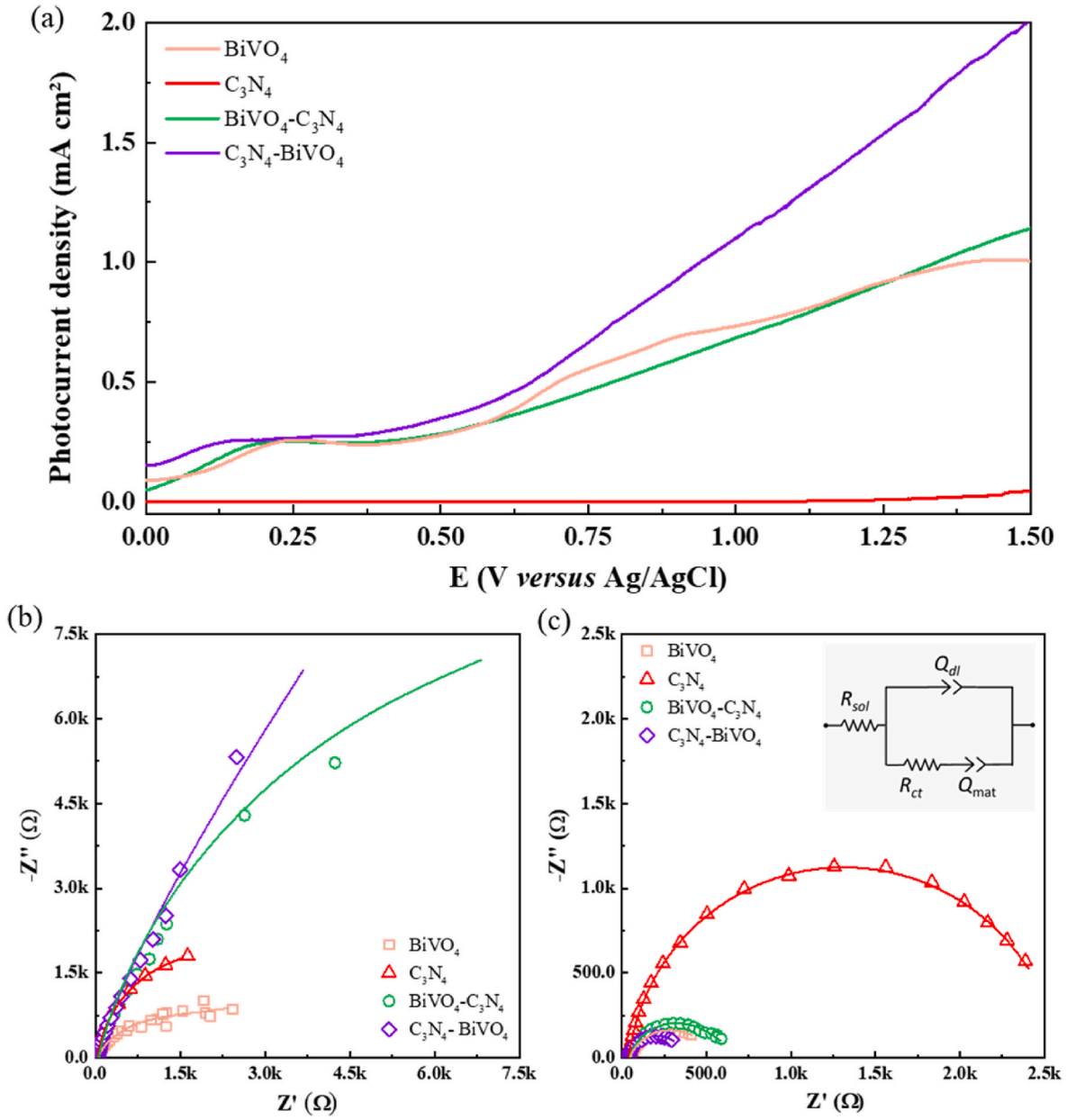

Fig. 3. (a) Linear voltammetry curves conducted at 5 mV s^{-1} from the composition electrodes in NaCl 60 mmol L^{-1} and Nyquist diagrams recorded photoanodes in the OER for (b) dark (c) light. As the inset figure, the Equivalent circuit is used for data adjustment.

to the pure electrodes, which indicates that the improved separation of photoexcited electrons/holes and the faster interfacial charge transfer occurred over the surface of the mixtures (Ansari et al., 2016). Additionally, it is important to comment that, in the dark, the heterostructures have a greater resistance to charge transfer when compared to the pure compounds. This occurs because the separation of the electron/hole pair needs light irradiation to occur and thus improve the performance of the materials. Thus, this result corroborates the linear voltammetry (Fig. S1), where heterostructures in the dark showed lower current density and OER onset at a higher potential.

After analyzing the physical and electrochemical characterizations, it was possible to observe that the material with the C_3N_4–$BiVO_4$ heterostructure has better physical and electrochemical properties when compared to other materials. Due to the promising efficiency, this material was applied in the degradation of a real effluent to analyze the viability of a future industrial application.

3.2. Photoelectrocatalytic detoxification using C_3N_4–$BiVO_4$ heterostructure

The application of photoelectrocatalysis for treating real effluents is a great challenge since they are extremely complex matrices. Here, the C_3N_4–$BiVO_4$ photoanode was chosen due to the better photoelectrocatalytical properties aiming at the degradation and detoxification of a real effluent provided by the textile industry. The real effluent provided for the study consists of wastewater from washing, bleaching, dyeing, tanning, and degumming processes in the textile industry. The effluent treatment experiments were conducted in an electrochemical cell, and the applied current was varied by 0.5, 1, and 2 mA cm^{-2}. Finally, the mineralization efficiency was evaluated from the amount of total organic carbon removed (Fig. 4), where all experiments were performed in triplicate.

In Fig. 4a it is possible to observe the mineralization degree after treatment at different current densities. Note that the

photoelectrochemical degradation at 1.0 mA cm^{-2} could remove more organic matter (55 %). Still, it can be stated that 0.5 mA cm^{-2} is not a sufficient current density to conduct this reaction; there was only 7 % removal of organic matter. On the other hand, increasing current density to 2 mA cm^{-2} led to lower TOC removal (40 %), probably due to the preferential occurrence of undesirable parallel reactions (for example, the evolution of oxygen and the oxidation of active chlorine to ClO_3^- and ClO_4^-) instead of oxidation reactions. Additionally, energy consumption was calculated based on the removed TOC. It is observed that the experiment conducted with a current density of 1 mA cm^{-2} needs less energy to remove a greater amount of organic matter.

In Fig. 4b, it is possible to observe the decay of TOC as a function of experiment time. Thus, it is possible to state that over time, around 55 % of the initial TOC was removed. Furthermore, the results obtained were adjusted to the kinetic model, and, as can be seen in Fig. 4c, the degradation of the real effluent adjusted well to the kinetics of the pseudo-first-order reaction. It is also important to mention that the removal of organic compounds present in the real matrix can occur through two different mechanisms. A direct route, where strong radicals (mainly •Cl and •OH) are formed on the surface of the electrode by photoexcitation from simulated solar irradiation, and the organic compound diffuses to the surface of the anode, where the strong radicals oxidize it formed (Young et al., 2018). An indirect route is still possible since it was observed that there is around 20 ppm of chlorine in the textile effluent (table s1), mainly due to the action of HClO/ClO (Dória et al., 2023), formed by the chlorine evolution reaction. A representative figure of the mechanisms can be seen in Fig. S2. Finally, the reuse of the C_3N_4–$BiVO_4$ film was studied by repeating the degradation of the real effluent for four cycles applying 1 mA cm^{-2} during 5h, using the same electrode. As depicted in Fig. 4d, the degradation percentage is reduced by about 10 % after the second cycle and 30 % after the fourth cycle, indicating satisfactory reusability and stability for the C_3N_4–$BiVO_4$ film.

Mane et al. (2022) synthesized a $BiVO_4$ decorated with C_3N_4 nanosheets. In simulated lighting, they obtained a photocurrent of 1.14 mA cm^{-2}, and the material was applied to the degradation of a model dye, methyl orange. By applying 1.23V for 75 min, they removed the color of a dye, which does not mean removing the dye. To confirm that the dye was removed, chromatographic measurements would be necessary. Thus, directly comparing these results is difficult due to the different experimental conditions tested. Table 2 summarizes the experimental conditions and the main reported results in treating real textile effluents.

The reduction of toxicity after the treatment of effluents is crucial in the direction of achieving a real application of electrochemical technology. Only organic compound removal is often assessed, and toxicity assessment is underestimated in this effluent. Thus, determining a substance's toxic potential by measuring a living organism's response using ecotoxicity tests allows us to evaluate the possibility of reuse of the treated water, for example, for crop irrigation. Therefore, it is extremely important to evaluate the detoxification capability of the proposed photoelectrochemical system to treat real textile effluent. At this point, under optimal operational conditions, the ecotoxicity of the effluent was evaluated using *L. Sativa*. Thus, as the reaction conducted by applying only 1 mA cm^{-2} achieved a satisfactory removal of more than 50 % of TOC, the ecotoxicity was evaluated before and after the treatment (Fig. 5).

Fig. 5 shows the GI and (RGI) before and after treatment. According to the literature, when the GI values obtained are between 0 and 40 %, 40–80 %, and 80–120 %, respectively, severe, mild, and insignificant inhibitions are considered (Assis et al., 2022; A. R. Dória et al., 2020a,b). High GI and RGI are observed after treatment; thus, the effluent was extremely toxic, with severe inhibition before treatment. After treatment, the inhibition became non-significant. The results showed that the synthesized electrodes efficiently remove organics in real effluents, and their by-products are not toxic to the environment.

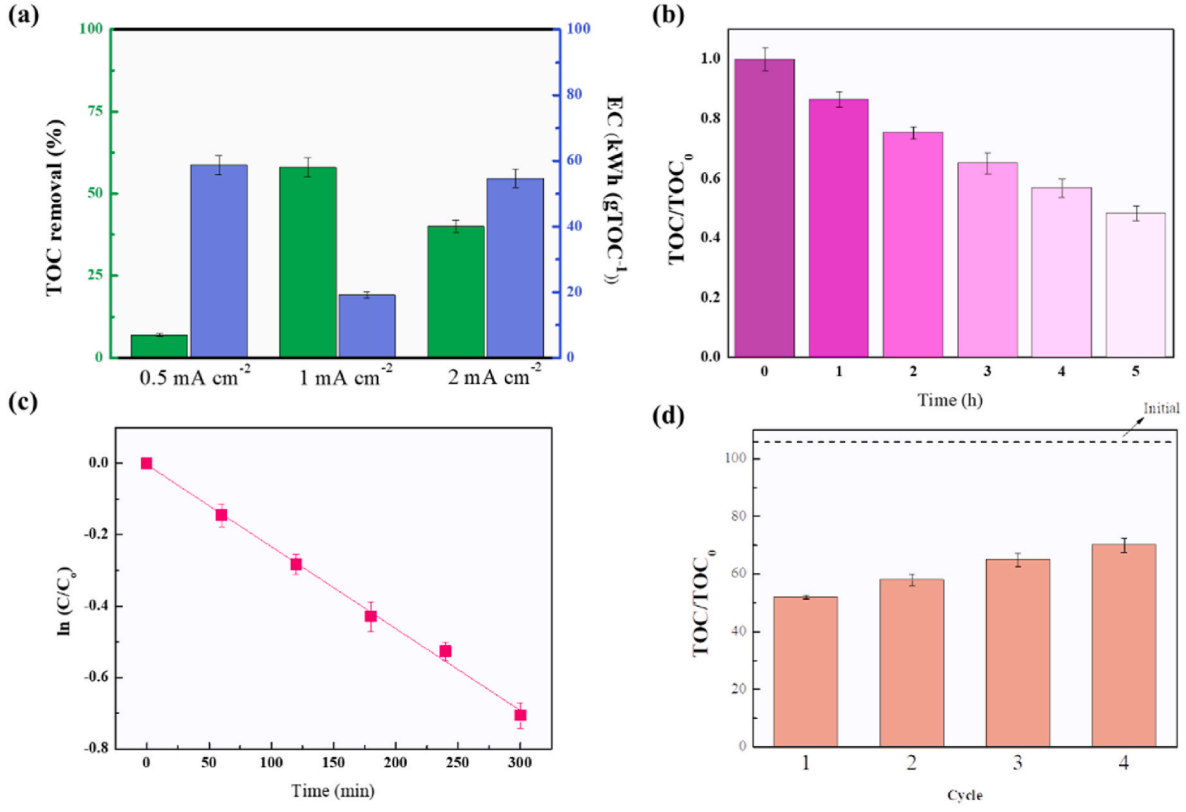

Fig. 4. (a) TOC removal from real effluent and energy consumption per mg of TOC removed in 5h. (b) TOC removal by applying 1 mA cm^{-2} (c) TOC decomposition kinetics versus treatment time by applying 1 mA cm^{-2} (d) Recycling of the C_3N_4–$BiVO_4$ electrode for treatment of real effluent from the textile industry in 5h in each cycle.

Table 2
Comparison of the performance of different systems for the degradation of the effluent textile industry.

Process	Anode	Conditions	Removal	Reference
EPhA	TiO_2/Ti	Pollutant: RTE +0.1 M NaCl E = 1V T = 150 min Irradiation: UV 250W	20 % TOC	Zainal et al. (2007)
EPhA	$Ti/Ru_{0.3}Ti_{0.7}O_2$	Pollutant: RTE + 0.1 M NaCl *j*: 40 mA cm^{-2} T = 600 min Irradiation: UV 250W	61 % color 64 % DQO	Alves et al. (2014)
EPhA	$Ti/Ru_{0.3}Ti_{0.\ 7}O_2$	Pollutant: STE *j*: 1 mA cm^{-2} T:300 min Irradiation: UV	90 % TOC 86 % DQO	de Mello Florêncio et al. (2016)
SPEF	DDB	Pollutant: RTE pH: 4 j: 40 mA cm^{-2} T:30 min Fe^{2+}:0.3 mM. Irradiation: Solar	70 % TOC 80 % DQO	GilPavas et al. (2018)
PhEC	$BiVO_4$/g-C_3N_4	Pollutant: Dye *j*: 1.34 mA cm^{-2} T: 75 min Irradiation: Solar simulation	90 % color	Mane et al. (2022)
PhEC	C_3N_4–$BiVO_4$	Pollutant: RTE pH:6.8 *j*: 1 mA cm^{-2} T: 300 min Irradiation: Solar simulation	55 % TOC ~100 % Toxicity	This Work

EPhA: Electrochemical Photo-assisted; RTE: Real Textile Efluente; STE: Simulated Textile Efluente E: Potential Applied; Solar Photo ElectroFenton; PhEC: Photoelectrochemical.

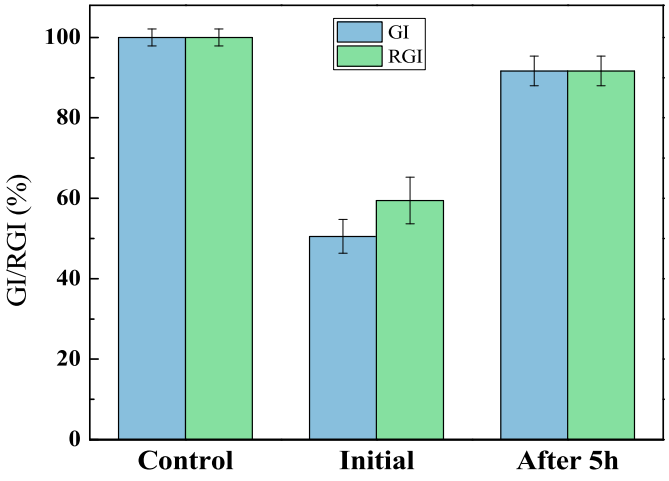

Fig. 5. Ecotoxicity assessment of real effluent with *Lactuca Sativa* before and after 5h treatment applying 1.0 mA cm^{-2} of current.

As evidenced in Tables 2 and it is noteworthy that only a few works focused on the treatment of real effluents from the textile industry. It is still possible to observe that, applying low current density, the results are excellent since it removes more than 50 % of the TOC and yields degradation products with lower toxicity compared to the effluent. Thus, it is possible to state that it is an attractive material for use in industrial applications since it is easily synthesized with low-cost materials that are abundant in the environment.

4. Conclusions

This study reported the successful synthesis of heteorstructures containing $BiVO_4$ and C_3N_4 using spin coating for deposition. The deposited thin films were homogeneous, regardless of the materials' composition and order of deposition. However, it was possible to observe that when C_3N_4 was deposited first and followed by $BiVO_4$, the photoanode showed better electrochemical properties, such as photocurrent density. Still, the heterostructures have a higher charge transfer constant value when evaluating the charge transfer than pure materials. On the other hand, when calculating the charge carriers, it was possible to detect that the charge mobility increased more than 10-fold in the C_3N_4– $BiVO_4$ compared to the $BiVO_4$–C_3N_4. Thus, due to its excellent characteristics, the C_3N_4–$BiVO_4$ photoanode was applied in the photoelectrochemical degradation and detoxification of a real effluent from the textile industry, applying 1 mA cm^{-2} of current density. When carrying out the tests, a photodegradation of ~50 % of TOC and a drastic reduction in effluent toxicity were assessed towards *L. Sativa*. Thus, it is possible to affirm that the photoanode proposed in the photoelectrochemical system is very efficient in removing organic pollutants from complex effluents, especially at very low current densities compared to other works in the literature. Therefore, it is a competitive material and sustainable for industrial applications.

Ethics approval

Not applicable.

Consent to participate

Not applicable (this study does not contain any individual person's data in any form).

Consent for publication

The authors declare that they agree with the publication of this paper in this journal.

CRediT authorship contribution statement

Isabelle M.D. Gonzaga: Writing – original draft, Methodology, Investigation, Funding acquisition, Formal analysis, Data curation. **Roger Gonçalves:** Writing – original draft, Methodology, Investigation, Formal analysis. **Carlos H.M. Fernandes:** Methodology, Investigation, Formal analysis. **Marcelo Assis:** Methodology, Investigation, Formal analysis. **Ivo F. Teixeira:** Writing – review & editing, Supervision, Conceptualization. **Lucia H. Mascaro:** Writing – review & editing, Supervision, Project administration, Funding acquisition, Conceptualization.

Declaration of competing interest

The authors declare that they have no known competing financial interests or personal relationships that could have appeared to influence the work reported in this paper.

Data availability

Data will be made available on request.

Acknowledgments

This research was funded by Fundação de Amparo a Pesquisa do Estado de São Paulo, FAPESP, grant number #2020/15211-0, #2020/14741-6, #2017/11986-5 and # 2013/07296-2. The Conselho Nacional de Desenvolvimento Científico e Tecnológico, CNPq, grant number #152607/2022-6, #311769/2022-5 and #406156/2022-0, Financiadora de Estudos e Projetos (FINEP) #grant number 01.22.0179.00. The authors also thank Shell for the strategic importance of the support given by ANP (Brazil's National Oil, Natural Gas, and Biofuels Agency) through the R&D levy regulation. M.A. was supported by the Margarita Salas postdoctoral contract MGS/2021/21 (UP2021-021) financed by the European Union-Next Generation EU.

Appendix A. Supplementary data

Supplementary data to this article can be found online at https://doi.org/10.1016/j.chemosphere.2024.141315.

References

Aguilera-Ruiz, E., De La Garza-Galván, M., Zambrano-Robledo, P., Ballesteros-Pacheco, J.C., Vazquez-Arenas, J., Peral, J., García-Pérez, U.M., 2017. Facile synthesis of visible-light-driven $Cu_2O/BiVO_4$ composites for the photomineralization of recalcitrant pesticides. RSC Adv. https://doi.org/10.1039/c7ra08513c.

Ali, S., Li, Z., Chen, S., Zada, A., Khan, I., Khan, I., Ali, W., Shaheen, S., Qu, Y., Jing, L., 2019. Synthesis of activated carbon-supported TiO_2-based nano-photocatalysts with well recycling for efficiently degrading high-concentration pollutants. Catal. Today. https://doi.org/10.1016/j.cattod.2019.03.044.

Alves, P.A., Johansen, H.D., Neto, S.A., De Andrade, A.R., De Jesus Motheo, A., Malpass, G.R.P., 2014. Photo-Assisted electrochemical degradation of textile effluent to reduce organic halide (AOX) production. Water. Air. Soil Pollut. https://doi.org/10.1007/s11270-014-2144-1.

Ansari, S.A., Ansari, M.O., Cho, M.H., 2016. Facile and scale up synthesis of red phosphorus-graphitic carbon nitride heterostructures for energy and environment applications. Sci. Rep. https://doi.org/10.1038/srep27713.

Assis, M., da Silva, J.S., Gonçalves, M.O., de Almeida Rodolpho, J.M., de Lima Fragelli, B. D., Corte, A.B.P., Ribeiro, L.K., Teodoro, M.D., de Freitas Anibal, F., de Sousa, C.P., Oliveira, O.N., Andrés, J., Longo, E., 2022. Bactericidal activity of $Ag_4V_2O_7/\beta$-$AgVO_3$ heterostructures against antibiotic-resistant Klebsiella pneumoniae. Biomater. Adv. 141 https://doi.org/10.1016/j.bioadv.2022.213097.

Bisquert, J., Zaban, A., Greenshtein, M., Mora-Seró, I., 2004. Determination of rate constants for charge transfer and the distribution of semiconductor and electrolyte electronic energy levels in dye-sensitized solar cells by open-circuit photovoltage decay method. J. Am. Chem. Soc. https://doi.org/10.1021/ja047311k.

Cao, J., Zhou, C., Lin, H., Xu, B., Chen, S., 2013. Surface modification of m-$BiVO_4$ with wide band-gap semiconductor BiOCl to largely improve the visible light induced photocatalytic activity. Appl. Surf. Sci. https://doi.org/10.1016/j.apsusc.2013.07.092.

Cao, S., Low, J., Yu, J., Jaroniec, M., 2015. Polymeric photocatalysts based on graphitic carbon nitride. Adv. Mater. 27, 2150–2176. https://doi.org/10.1002/adma.201500033.

Cao, Y., Wu, W., Wang, S., Peng, H., Hu, X., Yu, Y., 2016. Monolayer g-C_3N_4 fluorescent sensor for sensitive and selective colorimetric detection of silver ion from aqueous samples. J. Fluoresc. https://doi.org/10.1007/s10895-016-1764-9.

Chowdhury, A., Balu, S., Lan, K.-W., Wei-Chih Lee, L., Yang, T.C.-K., 2023. Synergistic effect of $BiVO_4$/P-g-C_3N_4 heterojunction with enhanced optoelectronic properties on synthetic colorants under visible light. Colorants. https://doi.org/10.3390/colorants2020019.

Corradini, P.G., De Brito, J.F., Boldrin Zanoni, M.V., Mascaro, L.H., 2020. Artificial photosynthesis for alcohol and 3-C compound formation using $BiVO_4$-lamelar catalyst. J. CO2 Util. https://doi.org/10.1016/j.jcou.2019.10.020.

de Araújo, M.A., Coelho, D., Mascaro, L.H., Pereira, E.C., 2018. The iron oxyhydroxide role in the mediation of charge transfer for water splitting using bismuth vanadate photoanodes. J. Solid State Electrochem. 22, 1539–1548. https://doi.org/10.1007/s10008-017-3774-1.

de Mello Florêncio, T., de Araújo, K.S., Antonelli, R., de Toledo Fornazari, A.L., da Cunha, P.C.R., da Silva Bontempo, L.H., de Jesus Motheo, A., Granato, A.C., Malpass, G.R.P., 2016. Photo-assisted electrochemical degradation of simulated textile effluent coupled with simultaneous chlorine photolysis. Environ. Sci. Pollut. Res. https://doi.org/10.1007/s11356-016-6912-x.

Dong, G., Zhang, Y., Pan, Q., Qiu, J., 2014. A fantastic graphitic carbon nitride (g-C3N4) material: electronic structure, photocatalytic and photoelectronic properties. J. Photochem. Photobiol. C Photochem. Rev. https://doi.org/10.1016/j.jphotochemrev.2014.04.002.

Dória, A.R., Gonzaga, I.M.D., Santos, G.O.S., Almeida, C.V.S., Silva, D.C., Silva, R.S., Romão, L.P.C., Sáez, C., Salazar-Banda, G.R., Eguiluz, K.I.B., 2023. Strong influence of the heating method on Ti/RuO_2-TiO_2 anode electrochemical and photoassisted electrochemical performance. Appl. Catal. B Environ. https://doi.org/10.1016/j.apcatb.2023.123092.

Dória, A.R., Pupo, M., Santos, G. de O.S., Vilar, D. da S., Torres, N.H., Romanholo Ferreira, L.F., Cavalcanti, E.B., Eguiluz, K.I.B., Salazar-Banda, G.R., 2020a. Electrochemical oxidation of indanthrene blue dye in a filter-press flow reactor and toxicity analyses with Raphidocelis subcapitata and Lactuca sativa. Ecotoxicol. Environ. Saf. https://doi.org/10.1016/j.ecoenv.2020.110659.

Dória, A.R., Silva, R.S., Oliveira Júnior, P.H., dos Santos, E.A., Mattedi, S., Hammer, P., Salazar-Banda, G.R., Eguiluz, K.I.B., 2020b. Influence of the RuO_2 layer thickness on the physical and electrochemical properties of anodes synthesized by the ionic liquid method. Electrochim. Acta. https://doi.org/10.1016/j.electacta.2020.136625.

Fernandes, C.H.M., Silva, B.F., Aquino, J.M., 2021. On the performance of distinct electrochemical and solar-based advanced oxidation processes to mineralize the insecticide imidacloprid. Chemosphere. https://doi.org/10.1016/j.chemosphere.2021.130010.

Garcia-Belmonte, G., Munar, A., Barea, E.M., Bisquert, J., Ugarte, I., Pacios, R., 2008. Charge carrier mobility and lifetime of organic bulk heterojunctions analyzed by impedance spectroscopy. Org. Electron. https://doi.org/10.1016/j.orgel.2008.06.007.

Garcia-Segura, S., Brillas, E., 2016. Combustion of textile monoazo, diazo and triazo dyes by solar photoelectro-Fenton: decolorization, kinetics and degradation routes. Appl. Catal. B Environ. https://doi.org/10.1016/j.apcatb.2015.08.042.

GilPavas, E., Dobrosz-Gómez, I., Gómez-García, M.Á., 2018. Optimization of solar-driven photo-electro-Fenton process for the treatment of textile industrial wastewater. J. Water Process Eng. https://doi.org/10.1016/j.jwpe.2018.05.007.

Gonçalves, R., Lima, T.M., Paixão, M.W., Pereira, E.C., 2018. Pristine carbon nitride as active material for high-performance metal-free supercapacitors: simple, easy and cheap. RSC Adv. https://doi.org/10.1039/c8ra06656f.

Gonzaga, I.M.D., Moratalla, A., Eguiluz, K.I.B., Salazar-Banda, G.R., Cañizares, P., Rodrigo, M.A., Saez, C., 2021. Outstanding performance of the microwave-made MMO-Ti/$RuO_2Ir O_2$ anode on the removal of antimicrobial activity of Penicillin G by photoelectrolysis. Chem. Eng. J. https://doi.org/10.1016/j.cej.2021.129999.

Gromboni, M.F., Araújo, M.A., Downey, E., Marken, F., Mascaro, L.H., 2016. Photoanodes on Titanium Substrates : One-step Deposited $BiVO_4$ versus Two-step Nano-V_2o_5 Films Impregnated with Bi^{3+} 273–283. https://doi.org/10.1007/s10008-015-3034-1.

Gutierrez-Urbano, I., Villen-Guzman, M., Perez-Recuerda, R., Rodriguez-Maroto, J.M., 2021. Removal of polycyclic aromatic hydrocarbons (PAHs) in conventional drinking water treatment processes. J. Contam. Hydrol. https://doi.org/10.1016/j.jconhyd.2021.103888.

Kang, J., Zhang, H., Duan, X., Sun, H., Tan, X., Liu, S., Wang, S., 2019. Magnetic Ni-Co alloy encapsulated N-doped carbon nanotubes for catalytic membrane degradation of emerging contaminants. Chem. Eng. J. https://doi.org/10.1016/j.cej.2019.01.035.

Karthik, P., Naveen Kumar, T.R., Neppolian, B., 2020. Redox couple mediated charge carrier separation in g-C_3N_4/CuO photocatalyst for enhanced photocatalytic H_2 production. Int. J. Hydrogen Energy 45, 7541–7551. https://doi.org/10.1016/j.ijhydene.2019.06.045.

Li, H., Zhou, L., Wang, L., Liu, Y., Lei, J., Zhang, J., 2015. In situ growth of TiO_2 nanocrystals on g-C_3N_4 for enhanced photocatalytic performance. Phys. Chem. Chem. Phys. https://doi.org/10.1039/c5cp02554k.

Li, X., Fang, G., Tian, Q., Wu, T., 2022. Crystal regulation of $BiVO_4$ for efficient photocatalytic degradation in g-C_3N_4/$BiVO_4$ heterojunction. Appl. Surf. Sci. https://doi.org/10.1016/j.apsusc.2022.152642.

Liang, X., Wang, G., Huo, T., Dong, X., Wang, G., Ma, H., Liang, H., Zhang, X., 2019. Band structure modification of g-C_3N_4 for efficient heterojunction construction and enhanced photocatalytic capability under visible light irradiation. Catal. Commun. https://doi.org/10.1016/j.catcom.2019.01.003.

Lu, G., Lun, Z., Liang, H., Wang, H., Li, Z., Ma, W., 2019. In situ fabrication of $BiVO_4$-$CeVO_4$ heterojunction for excellent visible light photocatalytic degradation of levofloxacin. J. Alloys Compd. https://doi.org/10.1016/j.jallcom.2018.09.064.

Ma, M., E, L., Zhao, D., Xin, Y., Wu, X., Meng, Y., Liu, Z., 2022. The p-n heterojunction of $BiVO_4/Cu_2O$ was decorated by plasma Ag NPs for efficient photoelectrochemical degradation of Rhodamine B. Colloids Surfaces A Physicochem. Eng. Asp. https://doi.org/10.1016/j.colsurfa.2021.127834.

Mane, P., Bae, H., Burungale, V., Lee, S.W., Misra, M., Parbat, H., Kadam, A.N., Ha, J.S., 2022. Interface-engineered Z-scheme of $BiVO_4$/g-C_3N_4 photoanode for boosted photoelectrochemical water splitting and organic contaminant elimination under solar light. Chemosphere. https://doi.org/10.1016/j.chemosphere.2022.136166.

Mascaro, L.H., Pockett, A., Mitchels, J.M., Peter, L.M., Cameron, P.J., Celorrio, V., Fermin, D.J., Sagu, J.S., Wijayantha, K.G.U., Kociok-Köhn, G., Marken, F., 2014. One-step preparation of the $BiVO_4$ film photoelectrode. J. Solid State Electrochem. 19, 31–35. https://doi.org/10.1007/s10008-014-2495-y.

Pingmuang, K., Chen, J., Kangwansupamonkon, W., Wallace, G.G., Phanichphant, S., Nattestad, A., 2017. Composite photocatalysts containing $BiVO_4$ for degradation of cationic dyes. Sci. Rep. https://doi.org/10.1038/s41598-017-09514-5.

Renda, C.G., Goulart, L.A., Fernandes, C.H.M., Mascaro, L.H., De Aquino, J.M., Bertholdo, R., 2021. Novel onion-like carbon structures modified with iron oxide as photocatalysts for the degradation of persistent pollutants. J. Environ. Chem. Eng. https://doi.org/10.1016/j.jece.2020.104934.

Rodriguez-Mozaz, S., Ricart, M., Köck-Schulmeyer, M., Guasch, H., Bonnineau, C., Proia, L., de Alda, M.L., Sabater, S., Barceló, D., 2015. Pharmaceuticals and pesticides in reclaimed water: efficiency assessment of a microfiltration-reverse osmosis (MF-RO) pilot plant. J. Hazard Mater. https://doi.org/10.1016/j.jhazmat.2014.09.015.

Rohloff, M., Anke, B., Wiedemann, D., Ulpe, A.C., Kasian, O., Zhang, S., Scheu, C., Bredow, T., Lerch, M., Fischer, A., 2019. Synthesis and doping strategies to improve the photoelectrochemical water oxidation activity of $BiVO_4$ photoanodes. Zeitschrift fur Phys. Chemie 234, 655–682. https://doi.org/10.1515/zpch-2019-1476.

Sharma, S.K., Kumar, A., Sharma, G., Naushad, M., Vo, D.V.N., Alam, M., Stadler, F.J., 2020. Fe_3O_4 mediated Z-scheme $BiVO_4/Cr_2V_4O_{13}$ strongly coupled nano-heterojunction for rapid degradation of fluoxetine under visible light. Mater. Lett. https://doi.org/10.1016/j.matlet.2020.128650.

Silva, I.F., Teixeira, I.F., Rios, R.D.F., do Nascimento, G.M., Binatti, I., Victória, H.F.V., Krambrock, K., Cury, L.A., Teixeira, A.P.C., Stumpf, H.O., 2021. Amoxicillin photodegradation under visible light catalyzed by metal-free carbon nitride: an investigation of the influence of the structural defects. J. Hazard Mater. https://doi.org/10.1016/j.jhazmat.2020.123713.

Starukh, H., Praus, P., 2020. Doping of graphitic carbon nitride with non-metal elements and its applications in photocatalysis. Catalysts. https://doi.org/10.3390/catal10101119.

Sun, J., Guo, Y., Wang, Y., Cao, D., Tian, S., Xiao, K., Mao, R., Zhao, X., 2018. H_2O_2 assisted photoelectrocatalytic degradation of diclofenac sodium at g-C_3N_4/$BiVO_4$ photoanode under visible light irradiation. Chem. Eng. J. https://doi.org/10.1016/j.cej.2017.09.041.

Thalluri, S.R.M., Martinez-Suarez, C., Virga, A., Russo, N., Saracco, G., 2013. Insights from crystal size and band gap on the catalytic activity of monoclinic $BiVO_4$. Int. J. Chem. Eng. Appl. https://doi.org/10.7763/ijcea.2013.v4.315.

Torabi, A., Staroverov, V.N., 2015. Band gap reduction in ZnO and ZnS by creating layered ZnO/ZnS heterostructures. J. Phys. Chem. Lett. https://doi.org/10.1021/acs.jpclett.5b00687.

Wang, H., Zhang, X., Xie, J., Zhang, J., Ma, P., Pan, B., Xie, Y., 2015. Structural distortion in graphitic-C_3N_4 realizing an efficient photoreactivity. Nanoscale. https://doi.org/10.1039/c4nr07645a.

Wang, J., Wang, S., 2018. Microbial degradation of sulfamethoxazole in the environment. Appl. Microbiol. Biotechnol. https://doi.org/10.1007/s00253-018-8845-4.

Wang, J., Zhuan, R., 2020. Degradation of antibiotics by advanced oxidation processes: an overview. Sci. Total Environ. https://doi.org/10.1016/j.scitotenv.2019.135023.

Wang, S., Wang, J., 2019. Activation of peroxymonosulfate by sludge-derived biochar for the degradation of triclosan in water and wastewater. Chem. Eng. J. https://doi.org/10.1016/j.cej.2018.09.062.

Wang, Y., Chen, D., Zhang, J., Balogun, M.S., Wang, P., Tong, Y., Huang, Y., 2022. Charge relays via dual carbon-actions on nanostructured $BiVO_4$ for high performance photoelectrochemical water splitting. Adv. Funct. Mater. https://doi.org/10.1002/adfm.202112738.

Wu, D., Li, J., Guan, J., Liu, C., Zhao, X., Zhu, Z., Ma, C., Huo, P., Li, C., Yan, Y., 2018. Improved photoelectric performance via fabricated heterojunction g-C_3N_4/TiO_2/HNTs loaded photocatalysts for photodegradation of ciprofloxacin. J. Ind. Eng. Chem. https://doi.org/10.1016/j.jiec.2018.03.017.

Xie, Z., Chen, D., Zhai, J., Huang, Y., Ji, H., 2023. Charge separation via synergy of homojunction and electrocatalyst in $BiVO_4$ for photoelectrochemical water splitting. Appl. Catal. B Environ. https://doi.org/10.1016/j.apcatb.2023.122865.

Xie, Z., Yang, Y., Fang, L., Wang, Y., Ding, X., Yuan, G., Liu, J.M., 2019. Photovoltaic, photo-impedance, and photo-capacitance effects of the flexible (111) $BiFeO_3$ film. Appl. Phys. Lett. https://doi.org/10.1063/1.5120484.

Xu, Q., Huang, Q.S., Luo, T.Y., Wu, R.L., Wei, W., Ni, B.J., 2021. Coagulation removal and photocatalytic degradation of microplastics in urban waters. Chem. Eng. J. https://doi.org/10.1016/j.cej.2021.129123.

Young, T.R., Li, W., Guo, A., Korshin, G.V., Dodd, M.C., 2018. Characterization of disinfection byproduct formation and associated changes to dissolved organic matter during solar photolysis of free available chlorine. Water Res. https://doi.org/10.1016/j.watres.2018.09.022.

Yu, J., Kudo, A., 2006. Effects of structural variation on the photocatalytic performance of hydrothermally synthesized $BiVO_4$. Adv. Funct. Mater. https://doi.org/10.1002/adfm.200500799.

Yuan, Y., Guo, R., tang Hong, L., fei Ji, X., yin, Lin, dong Li, Z., sheng, Z., guo, Pan W., 2021. A review of metal oxide-based Z-scheme heterojunction photocatalysts: actualities and developments. Mater. Today Energy. https://doi.org/10.1016/j.mtener.2021.100829.

Zainal, Z., Lee, C.Y., Hussein, M.Z., Kassim, A., Yusof, N.A., 2007. Electrochemical-assisted photodegradation of mixed dye and textile effluents using TiO_2 thin films. J. Hazard Mater. https://doi.org/10.1016/j.jhazmat.2006.11.055.

Zhao, J., Yan, J., Jia, H., Zhong, S., Zhang, X., Xu, L., 2016. $BiVO_4$/g-C_3N_4 composite visible-light photocatalyst for effective elimination of aqueous organic pollutants. J. Mol. Catal. Chem. https://doi.org/10.1016/j.molcata.2016.08.025.

Zhong, X., Zhang, K.X., Wu, D., Ye, X.Y., Huang, W., Zhou, B.X., 2020. Enhanced photocatalytic degradation of levofloxacin by Fe-doped BiOCl nanosheets under LED light irradiation. Chem. Eng. J. https://doi.org/10.1016/j.cej.2019.123148.

Zhuang, S., Cheng, R., Wang, J., 2019. Adsorption of diclofenac from aqueous solution using UiO-66-type metal-organic frameworks. Chem. Eng. J. https://doi.org/10.1016/j.cej.2018.11.150.